Hydrodynamic interactions in metal rodlike-particle suspensions due to induced charge electroosmosis

Klint A. Rose,[1] Brendan Hoffman,[2] David Saintillan,[3] Eric S. G. Shaqfeh,[2,4] and Juan G. Santiago[4]
[1]*Meso, Micro, and Nanotechnology Center, Lawrence Livermore National Laboratory, Livermore, California 94550, USA*
[2]*Department of Chemical Engineering, Stanford University, Stanford, California 94305, USA*
[3]*Department of Mechanical Science and Engineering, University of Illinois at Urbana-Champaign, Urbana, Illinois 61801, USA*
[4]*Department of Mechanical Engineering, Stanford University, Stanford, California 94305, USA*
(Received 9 May 2008; revised manuscript received 19 November 2008; published 9 January 2009)

We present a theoretical and experimental study of the role of hydrodynamic interactions on the motion and dispersion of metal rodlike particles in the presence of an externally applied electric field. In these systems, the electric field polarizes the particles and induces an electroosmotic flow relative to the surface of each particle. The simulations include the effect of the gravitational body force, buoyancy, far-field hydrodynamic interactions, and near-field lubrication forces. The particles in the simulations and experiments were observed to experience repeated pairing interactions in which they come together axially with their ends approaching each other, slide past one another until their centers approach, and then push apart. These interactions were confirmed in measurements of particle orientations and velocities, pair distribution functions, and net dispersion of the suspension. For large electric fields, the pair distribution functions show accumulation and depletion regions consistent with many pairing events. For particle concentrations of 10^8 particles/mL and higher, dispersion within the suspension dramatically increases with increased field strength.

DOI: 10.1103/PhysRevE.79.011402 PACS number(s): 82.70.Dd, 82.45.−h

I. INTRODUCTION

Novel microfluidic applications of nanorods and microrods are currently under development. Nanorods or microrods are cylindrical particles with lengths ranging from tens of nanometers to tens of microns and diameters from a few nanometers up to a few microns. Metal microrods, fabricated from either a single homogenous material or with stripes of different metals along their length, can serve as identification tags in applications such as multiplexed biodetection assays [1,2]. Manipulation of individual rodlike metal particles, or suspensions of these particles enables control of their transport and orientation for identification or additional analysis. Electric fields are an appealing option for manipulating rodlike metal particles in solution because they are easily integrated into microfluidic devices.

When an electric field is applied to a rodlike metal particle in aqueous solution, the particle and the ionic double layer around it polarize as illustrated in Fig. 1(a). The metal particle initially polarizes in the applied field as electrons quickly redistribute themselves to maintain an equipotential at the particle surface. This initial stage of polarization results temporarily in an electric field perpendicular to the surface of the particle [Fig. 1(b)]. The field drives ions from the solution to the particle surface. Assuming the potential drop across the particle does not initiate electrochemical reactions, these ions accumulate within the electric double layer (EDL) near the particle surface. This charge builds up until the ionic-current-carrying electric field is expelled from the EDL [Fig. 1(c)] [3,4]. The external field then acts on mobile EDL ions, causing them to migrate towards the electrode of opposite charge. Ion drag induces flow of the liquid near the particle [4].

The electroosmotic flow at the surface of the particle moves liquid from the ends of the particle to its center resulting in a toroidal vortex velocity field that extends beyond the double layer. This induced charge electroosmosis (ICEO), described in detail by Bazant and Squires [5], was experimentally observed by Gamayunov *et al.* [6] around spherical metal particles and by Levitan *et al.* [7] around the cross section of a cylindrical wire. They measured velocities of tracer particles around the polarized objects and demonstrated a second order dependence on the electric field strength. These results qualitatively confirmed the ICEO flows predicted at the surface of conducting and dielectric spheres by Gamayunov *et al.* [8] and Murtsovkin [9] and cylinders by Squires and Bazant [4].

For asymmetrically charged (and asymmetric shaped) particles the electroosmotic flow in one direction can dominate,

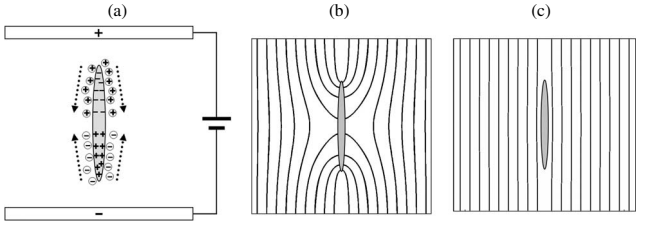

FIG. 1. Charging of an ideally polarizable prolate spheroid in a uniform electric field. (a) The charge in the metal particle (shaded region) is initially attracted to the electrode with opposite charge. Ions from the solution are driven to the surface of the particle by the dipole field and accumulate. These ions continue to move through the double layer towards the opposite electrode and drag fluid as they migrate. This motion generates a flow along the surface in the direction of the arrows. (b) Electric field lines initially intersect the conducting particle at right angles although no electrochemical reactions occur at the surface. (c) Electromigration of ions to the particle surface charges the double layer until the induced dipole is completely screened. The particle appears to be a perfect insulator with field lines parallel to the surface.

leading to net electrophoretic particle motion. Gamayunov and Murtsovkin [10], Murtsovkin and Mantrov [11], and Gangwal *et al.* [12] observed this motion for anisometric dielectric particles in alternating current (ac) fields and found that the velocity generally increased with the square of the field strength amplitude. Bazant and Squires [5] described this translational motion as induced charge electrophoresis (ICEP). For axisymmetric particles such as rodlike particles, the ICEO flow field is symmetric and leads to no net particle translation.

The ICEO flow around the particles produces increased hydrodynamic interactions between them. The overlapping ICEO liquid flow fields cause the particles to attract or repel one another depending on their relative positions. Gamayunov *et al.* [8] and Dukhin and Murtsovkin [13] analyzed the theoretical effects of the ICEO flow fields on the stability of spherical particles in suspension. Saintillan [14] analyzed the theoretical motion for a pair of spherical particles due to ICEO flows coupled with dielectrophoresis. Saintillan *et al.* [15,16] used slender body theory to simulate the ICEO driven hydrodynamic interactions of rodlike particles. They analyzed the pair distribution functions, diffusivities, settling velocities, and stability of the suspended particles.

Rose *et al.* [3,17] demonstrated the use of externally applied electric fields to manipulate (e.g., align) low concentrations of metal microrod particles in aqueous solutions. They studied the coupling of Brownian motion and rotational electrokinetic motion for individual particles (in suspensions with low particle concentrations). They presented models for particles with very thick and very thin electric double layers and validated their models with experiments tracking particle position and orientation. Their work was limited to particle concentrations n, on the order of 10^5 particles/mL or less. These concentrations are equivalent to an effective volume fraction (based on particle half-length c) of approximately $nc^3=3\times10^{-6}$. In such regimes, particle-particle interactions may be ignored, but as the concentration of the suspension increases these interactions must be taken into account. As we shall see below, critical volume fractions for significant particle-particle interaction are as low as $nc^3=6\times10^{-3}$.

In this paper, we present a theoretical and experimental study of particle motions in the regime of 10^8 to 10^9 particles/mL ($nc^3=6\times10^{-3}$ to 3×10^{-2}), where the primary particle-particle interaction is due to the hydrodynamic flow field generated around each particle. We first present theoretical results describing the polarization of a particle in an electric field and the resulting flow field generated around it. We also review the theoretical pair distribution function between two particles with ICEO flow fields at their surface, as first described by Saintillan *et al.* [15]. In Sec. IV, we present the results from particle suspension simulations which use the method described by Saintillan *et al.* [15] but with modifications to include an adaptive time step for close interactions between particles. We then describe our experiments to investigate particle-particle interactions for metal microrods under the same conditions. We compare the experimental and simulation results for particle velocities, pair distribution functions, and dispersion. We end with conclusions and recommendations in Sec. V.

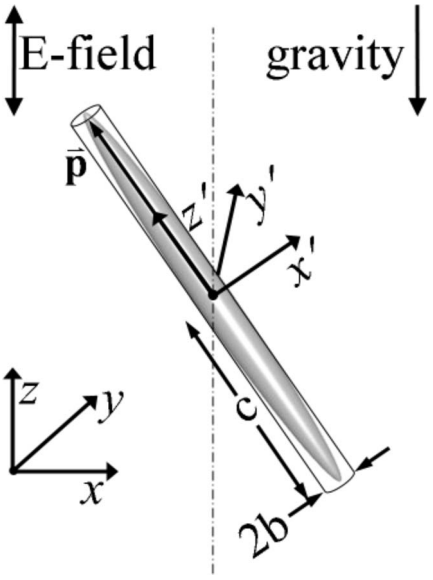

FIG. 2. Illustration of a rodlike particle modeled as a prolate spheroid and the relevant coordinate systems. The coordinate system $\mathbf{x}'$ is fixed to the particle with the z' coordinate parallel to the major axis (half-length, c) and the x' and y' coordinates parallel to the minor axes (half-length, b). The primary coordinate system $\mathbf{x}$ is fixed to the microfluidic channel with the z axis parallel to the gravitational vector and the x axis parallel to the image plane (y axis into the page). The unit vector $\mathbf{p}$ originates at the particle center and is parallel to the primary axis (z' direction). The vector describes the orientation of the particle with respect to the primary coordinate system. The applied ac field is parallel to gravity.

II. THEORY

This section describes a single-particle model, particle-pair model, and multiparticle suspension simulations for induced charge electroosmosis around perfectly polarizable rodlike metal particles. From the single particle model we determine the slip velocity generated at the particle surface due to the motion of ions within the polarized EDL. From this slip velocity, we calculate the liquid flow field around a single particle. The multiparticle simulations include the slip velocity due to ICEO as well as the gravitational body force, buoyancy, far-field hydrodynamic interactions, near-field lubrication forces, and Brownian forces. The simulations capture many particle interactions and provide measurements of the average particle velocity field and pair distribution function around the particles as well as dispersion within the suspension.

A. Single particle model

We model a cylindrical particle with length L and radius r as a prolate spheroid with characteristic half-lengths $c=L/2$ and $b=r$. As shown in Fig. 2, we define the particle coordinate system $\mathbf{x}'$ with components x' and y' aligned with the two minor axes (with equal lengths b) and z' aligned with the major axis (length c) of the particle. We define a unit orientation vector $\mathbf{p}$ directed from the center of the particle along the primary axis of the particle. The vector $\mathbf{x}$ describes

the channel coordinate system with the x and y components aligned perpendicular and the z component aligned parallel to the direction of gravity, respectively. The electric field direction is parallel to the gravitational vector as well.

We assume the characteristic thickness of the electric double layer, defined as

$$\lambda_D = \left(\frac{\varepsilon_m kT}{2e^2 z_\pm^2 n_\infty} \right)^{1/2} \tag{1}$$

for a symmetric electrolyte, is thin such that $\lambda_D \ll b$. Here ε_m is the permittivity of the fluid, k is the Boltzmann constant, T is temperature, e is electron charge, $z_\pm$ is the valence of the ions in a binary electrolyte solution, and n_∞ is the number density of ions in the bulk solution.

A nonuniform potential near the particle surface, referred to as the induced zeta potential, characterizes the polarized double layer. To solve for this zeta potential, we use the approach described by Squires and Bazant [4]. When the field is initially applied, we assume the particle acts as a perfect conductor [Fig. 1(b)] with all field lines perpendicular to the particle surface and surface potential $\phi_{\text{cond}}(S_p)$. This initial polarization occurs on the order of the relaxation time for the redistribution of electrons within the metal. This time scale, $\tau_c = \varepsilon_p / \sigma_p$ depends on the particle permittivity, ε_p and conductivity σ_p and is negligibly short for metals such as silver. Once the particle material itself is polarized, the electric field drives ions from the solution to the particle surface where they eventually shield the entire particle surface from the externally applied field [as if a perfect insulator, see Fig. 1(c)]. For thin EDLs, the resulting insulator potential $\phi_{\text{ins}}(S_p)$ can be defined at the outer edge of the double layer after it has polarized. Note that the particle with its polarized double layer acts as a perfectly polarizable insulator (with no perpendicular component of field) with respect to the external (net-current-carrying) field only. The internal field associated with the EDL is always normal to the metal surface. Section II C below describes the timescale for double layer polarization.

The induced zeta potential is defined as $\zeta_s = \phi_{\text{cond}}(S_p) - \phi_{\text{ins}}(S_p)$, and assuming no native surface charge, simplifies to

$$\zeta_s = \mathbf{x}' \cdot \mathbf{L} \cdot \mathbf{E}_\infty, \tag{2}$$

where $\mathbf{x}'$ is the distance vector from the particle center, $\mathbf{E}_\infty$ is the externally applied field, and $\mathbf{L}$ is the polarization tensor defined as

$$\mathbf{L} = \frac{\mathbf{pp}}{(1 - L_\parallel)} + \frac{\mathbf{I} - \mathbf{pp}}{(1 - L_\perp)} \tag{3}$$

with polarization factors L. The polarization factors, defined perpendicular and parallel to the primary axis, are

$$L_\perp = \frac{1}{2(1-\alpha^2)} - \frac{\alpha^2}{4(1-\alpha^2)^{3/2}} \ln\left(\frac{1 + (1-\alpha^2)^{1/2}}{1 - (1-\alpha^2)^{1/2}} \right), \tag{4a}$$

$$L_\parallel = -\frac{\alpha^2}{(1-\alpha^2)} + \frac{\alpha^2}{2(1-\alpha^2)^{3/2}} \ln\left(\frac{1 + (1-\alpha^2)^{1/2}}{1 - (1-\alpha^2)^{1/2}} \right), \tag{4b}$$

in terms of the aspect ratio $\alpha \equiv b/c$ $(c > b)$ [18,19].

The velocity at the slip plane near the particle surface is described by the Helmholtz-Smoluchowski equation

$$\mathbf{u}_s = -\frac{\varepsilon_m \zeta_s}{\eta} \mathbf{E}_s \tag{5}$$

with the induced zeta potential from Eq. (2) and the "local" tangential electric field $\mathbf{E}_s$. The tangential field is the gradient of the potential at the surface of the insulating particle and can be formulated in terms of the polarization tensor as

$$\mathbf{E}_s = -\nabla \phi_{\text{ins}} = (\mathbf{I} - \mathbf{nn}) \cdot \mathbf{L} \cdot \mathbf{E}_\infty, \tag{6}$$

where $\mathbf{n}$ is the unit vector normal to the surface. The resulting slip velocity at the surface of the particle is

$$\mathbf{u}_s(\mathbf{x}') = -\frac{\varepsilon}{\eta} (\mathbf{x}' \cdot \mathbf{L} \cdot \mathbf{E}_\infty)[(\mathbf{I} - \mathbf{nn}) \cdot \mathbf{L} \cdot \mathbf{E}_\infty] \tag{7}$$

which is quadratic with respect to $\mathbf{E}_\infty$ as expected for induced charge electroosmosis. If the particle is aligned with its orientation vector parallel to the field, the magnitude of the ICEO flow at the surface can be approximated as

$$u_{\text{ICEO}} = \frac{\varepsilon_m c E_\infty^2}{\eta}. \tag{8}$$

The potential drop across the particle half-length, cE_∞, provides an estimate of the magnitude of the induced zeta potential in this orientation.

We obtain the velocity field generated by the slip velocity at the particle surface by solving the Stokes equations

$$-\eta \nabla^2 \mathbf{u} + \nabla p = 0 \quad \text{and} \quad \nabla \cdot \mathbf{u} = 0 \tag{9a}$$

in the particle-based coordinate system $\mathbf{x}'$ with boundary conditions

$$\mathbf{u}(\mathbf{x}') = \mathbf{u}_{\text{ICEP}} + \boldsymbol{\omega}_{\text{ICEP}} \times \mathbf{x}' + \mathbf{u}_s(\mathbf{x}') \tag{9b}$$

at the slip plane (approximated as the particle surface for the thin EDL limit) and

$$\mathbf{u}(\mathbf{x}') \to 0 \tag{9c}$$

far from the particle [15]. The translational $\mathbf{u}_{\text{ICEP}}$ and rotational $\boldsymbol{\omega}_{\text{ICEP}}$ induced charge electrophoretic velocities are

$$\mathbf{u}_{\text{ICEP}} = -\frac{\varepsilon_m}{3 V_p \eta} \int \int_{S_p^+} (\mathbf{n} \cdot \mathbf{r}) \mathbf{E}_s \phi_{\text{ins}} dS \tag{10a}$$

and

$$\boldsymbol{\omega}_{\text{ICEP}} = -\frac{\varepsilon_m}{V_p \eta} \mathbf{G} \cdot \int \int_{S_p^+} (\mathbf{n} \cdot \mathbf{r}) \mathbf{r} \times \mathbf{E}_s \phi_{\text{ins}} dS, \tag{10b}$$

where $\mathbf{r}$ is the distance vector from the center of the particle, $\mathbf{G} = (2b^2)^{-1}\mathbf{pp} + (b^2 + c^2)^{-1}(\mathbf{I} - \mathbf{pp})$, and $V_p = 4/3 b^2 c$ is the volume of the particle.

There is no net translation due to induced charge electrophoresis for the axisymmetric rodlike particle modeled here; however, the particle will rotate to align in the field [3,15]. The analytical solution to Eqs. (9a)–(9c) is difficult to obtain due to the complex slip velocity around the spheroidal geometry. To demonstrate the flow field around a single par-

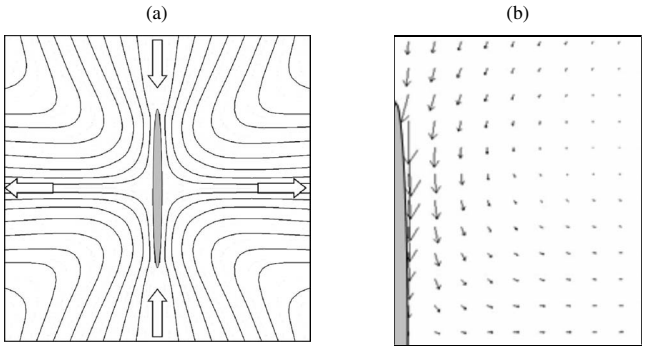

FIG. 3. Three-dimensional ICEO velocity field around a polarized spheroid particle shown at a slice along the primary particle axis. The flow field is radially symmetric about this axis. (a) Velocity streamlines around the particle demonstrating the quadrupolar flow field. The arrows indicate the direction of flow along the streamlines. (b) The vector field for the velocity in a single quadrant shows the fluid is drawn towards the particle at the ends and pushed away from the particle at the center.

ticle, we obtained the three-dimensional electric and velocity fields using a numerical finite element method (FEM) solver (Comsol, Palo Alto, CA) with the conductive media dc and Stokes flow toolboxes. Figure 3 shows the resulting velocity vectors and streamlines for a plane parallel to the primary axis. The velocity field is symmetric about the major and minor axes of the particle and is quadrupolar. The velocity vectors in Fig. 3(b) demonstrate that, for an aligned particle, liquid is pulled toward regions near the particle ends, and pushed away at its center.

B. Particle pair interactions

To understand the ICEO induced hydrodynamic interactions in a suspension of rodlike particles, we consider particle pair interactions as well as the net effects on dispersion. Particle pair interactions provide important information about the entire suspension. Of particular interest are the relative velocities of one particle with respect to another and the pair distribution function which describes the probability density function of finding a particle in a given location around another. Saintillan *et al.* [15] used slender body theory to derive expressions for the relative velocity and pair distribution function. We summarize their approach here.

The relative velocity describes the motion of a particle center in a reference frame fixed to the axis of another. Assuming the particles are both approximately aligned with the field, with their centers located at $\mathbf{x}_1$ and $\mathbf{x}_2$, the separation vector between the particle centers is defined as $\mathbf{x}_r=\mathbf{x}_2-\mathbf{x}_1$. The relative velocity of rod 2 with respect to rod 1 is simply $\mathbf{u}_r=\dot{\mathbf{x}}_2-\dot{\mathbf{x}}_1$. By mapping the relative velocity over various separation vectors, regions of attraction and repulsion can be determined for the particle pair. As mentioned previously, analytical solutions for the velocity field are difficult to obtain. Saintillan *et al.* [15] therefore used slender body theory, in which the velocity disturbance induced by a low aspect ratio ($b/c \ll 1$) particle is approximated by a line distribution of point force singularities along the particle axis. The slip velocity is then presented as a circumferential average at a location s along the length of the particle. The resulting slip velocity is

$$\tilde{\mathbf{u}}_s(s) \approx -\frac{\varepsilon_m}{\eta} s(\mathbf{p}\cdot\tilde{\mathbf{E}}_\infty)\tilde{\mathbf{E}}_\infty, \tag{11}$$

where the field is defined as

$$\tilde{\mathbf{E}}_\infty = \left(\frac{\mathbf{pp}}{1+L_\parallel} + \frac{\mathbf{I}-\mathbf{pp}}{2(1+L_\perp)}\right)\cdot\mathbf{E}_\infty \tag{12}$$

in terms of the orientation vector $\mathbf{p}$ along the axis of the slender body. This simplified slip velocity enables the calculation of relative particle velocities which are a function of the stresslet from the velocity disturbance. See Ref. [15] for details. The simplified slip velocity also enables calculation of the rotational velocity due to the induced charge electroosmosis at the particle surface. The simplified rotational velocity is

$$\boldsymbol{\omega}_{\mathrm{ICEP}} = \frac{\varepsilon_m}{\eta}\mathbf{p}\times\tilde{\mathbf{E}}_\infty(\mathbf{p}\cdot\tilde{\mathbf{E}}_\infty). \tag{13}$$

The pair distribution function in a suspension depends on the relative velocity between rods. High and low values are proportional to the probability of finding another particle; thereby denoting regions of most probable particle depletion and accumulation, respectively. Saintillan *et al.* [15] used the method of reflections to calculate the velocity of two particles perfectly aligned in the field with one particle fixed at the origin. The relative velocity is

$$\mathbf{u}_r = \frac{\varepsilon_m G_\parallel^2 E_\infty^2}{3\eta\ln(2/\alpha)}\left[(1-3\cos^2\theta)\frac{\mathbf{x}_r c^3}{|\mathbf{x}_r|^3} + O(|\mathbf{x}_r|^{-5})\right], \tag{14}$$

where $G_\parallel = 1/(1-L_\parallel)$ and $\cos\theta = (\mathbf{x}_r\cdot\mathbf{p}/|\mathbf{x}_r|)$. From this relative velocity, they calculated the pair distribution function which predicts accumulation near the ends of the particles, where the two rods are pulled together by the hydrodynamic flow. In contrast, the depletion region occurs near the center of the particles where the flow pushes them apart.

C. Dielectrophoresis effects

An additional component in the electrical interactions between perfectly polarizable metal particles is the dielectrophoretic (DEP) interaction of induced dipoles. The external field induces a dipole moment $\mathbf{a}$ in each particle equivalent to

$$\mathbf{a} = \frac{8}{3}\pi\varepsilon_m c^3\alpha^2\tilde{\mathbf{E}}_\infty, \tag{15}$$

which leads to a dielectrophoretic torque on the particle of $\mathbf{T}_{\mathrm{DEP}}=\mathbf{a}\times\mathbf{E}_\infty$ [15]. The rotational velocity due to the DEP torque is

$$\boldsymbol{\omega}_{\mathrm{DEP}} = \frac{\varepsilon_m\alpha^2\ln(2/\alpha)}{\eta}\tilde{\mathbf{E}}_\infty\times\mathbf{E}_\infty, \tag{16}$$

and is in the same direction as the rotation due to ICEP described in Eq. (13).

The induced dipoles also cause translational motion between the particles similar to the motion due to ICEO at the surface. The forces between the dipoles pull particles together at their ends and push the particles apart at their centers. To estimate the relative velocity between two particles due to this dipole-dipole force, we assume both particles are perfectly aligned parallel to the field and one particle is fixed at the origin. The dipole force on each particle when their centers are along the same horizontal plane is estimated as

$$\mathbf{F}_D = \frac{16}{3}\pi\varepsilon_m\alpha^4 G_\parallel^2 E_\infty^2(1-3\cos^2\theta)\frac{\mathbf{x}_r c^6}{|\mathbf{x}_r|^5}. \quad (17)$$

Balancing this force with the drag forces parallel and perpendicular to the particle's major axis provides an estimated velocity of

$$\mathbf{u}_D = \frac{4\varepsilon_m\alpha^4 G_\parallel^2 E_\infty^2 \ln(2/\alpha)}{3\eta}\left(\frac{1-3\cos^2\theta}{\cos\theta+2\sin\theta}\right)\frac{\mathbf{x}_r c^5}{|\mathbf{x}_r|^5}. \quad (18)$$

The relative contribution of DEP effects to the overall particle interactions depends on the frequency of the applied electric field compared to the charging dynamics of the electric double layer around the particles. The double layer polarizes on a time scale of $\tau_i=\varepsilon_m a/(\sigma_m\lambda_D)$, where ε_m and σ_m are permittivity and conductivity of the aqueous medium, λ_D is the Debye length defined in Eq. (1), and a is the characteristic length scale of the particle. This is effectively an *RC*-type charging time scale based on the resistance of the bulk medium and the capacitance across the electric double layer [20].

For frequencies above the critical frequency $f_c=1/\tau_i$ ions do not have sufficient time to accumulate at the particle surface and the effects due to ICEO are negligible. Instead, the DEP torque and dipole-dipole interaction dominate. Jamshidi *et al.* used this high-frequency regime to measure the dipole repulsion forces between silver nanowires in aqueous solutions. Their results agree well with a model similar to Eq. (18) [21].

At frequencies well below the critical frequency, induced charge electroosmosis effects dominate. The rotational velocity due to DEP [Eq. (16)] is a factor of $\alpha^2\ln(2/\alpha)$ weaker than the ICEP rotational velocity [Eq. (13)] in this regime. Similarly, the magnitude of the relative velocity for two particles in the same horizontal plane (i.e., $\theta=\pi/2$) is a factor of $2\alpha^4\ln(2/\alpha)^2$ smaller for dipole-dipole interactions [Eq. (18)] than for motion due to the induced charge electroosmotic flow at the surface [Eq. (14)]. The velocity due to the dipole-dipole interactions also decays much more rapidly with the distance between the particles (order $1/r^4$) than the ICEO velocity (order $1/r^2$).

For the particles and solutions of interest here, the double layer polarization time is on the order of 10^{-6} s and the critical frequency is approximately 1 MHz. For particles with an aspect ratio of 0.05 (radius/length), the ICEP rotational velocity is 100 times greater than DEP rotation and the magnitude of the ICEO relative velocity is more than 1000 times greater than the motion due to the induced dipoles. The DEP forces due to the induced dipole are therefore neglected in this study.

D. Suspension simulations

To capture many particle interactions we simulate periodic suspensions of large numbers of Brownian rodlike particles as described by Saintillan *et al.* [15,16]. The simulations include gravitational body force, buoyancy, far-field hydrodynamic interactions, and near field lubrication forces. The particle hydrodynamic interactions include the effects of induced charge electroosmosis. Close interactions between particles can occur during particle pairing events and as a consequence of differing (e.g., orientation-dependent) sedimentation speeds. To better capture these interactions, we modified the integration method of Saintillan *et al.* to replace the midpoint algorithm with a lower-order adaptive time step. In comparison to the implicit algorithm of Saintillan *et al.* [15,16], an explicit scheme with adaptive time stepping allows us to more easily resolve the dynamics associated with particle-particle interactions. In the current scheme, we adopt an intermediate time step (typically 1/100 of the full time step) to resolve the hydrodynamics and associated particle motion; while assuming a larger time step (typically ~50 ms) during which time the Brownian force is held constant. We therefore explicitly calculate the particle drift when necessary. Despite the additional calculation, the flexibility allowed by adaptive time stepping increases simulation speed. This adaptive time-stepping method was motivated by an algorithm developed by Banchio and Brady [22] and is described in detail in Ref. [23].

We use the slender body theory expression [Eq. (11)] for the slip velocity along the particle. Due to symmetry, the ac applied field results in zero net translation of the particles but does enhance alignment into the field [Eq. (10b)] and generates an electroosmotic slip velocity. To quantify the effects of this hydrodynamic disturbance on the suspension, we determine the pair distribution function by measuring the two-dimensional histogram of relative particle locations throughout the simulation. Varied parameters in the simulations include the volume fraction (nc^3) of particles and the Peclet number Pe. We define the Peclet number as the ratio of the advective flux due to the ICEO slip velocity along the particle [Eq. (8)] to the diffusive particle flux normal to its major axis, characterized by $D_\perp$. For a slender body, with aspect ratio $\alpha \ll 1$ (or $c \gg b$), the diffusion coefficient perpendicular to the particle's major axis is

$$D_\perp = \frac{kT\ln(2/\alpha)}{8\pi\eta c} \quad (19)$$

and the resulting Peclet number is

$$\mathrm{Pe} = \frac{u_{\mathrm{ICEO}}c}{D_\perp} = \frac{8\varepsilon_m E_\infty^2 \pi c^3}{kT\ln(2/\alpha)}. \quad (20)$$

Note that the Pe definition in Eq. (20) is a factor of 4 less than the value used in Refs. [15,16] due to their scaling by the full particle length instead of the particle half-length.

We also calculate the hydrodynamic dispersion for each simulation. The hydrodynamic dispersion is an effective diffusion coefficient that accounts for an increase in the mean

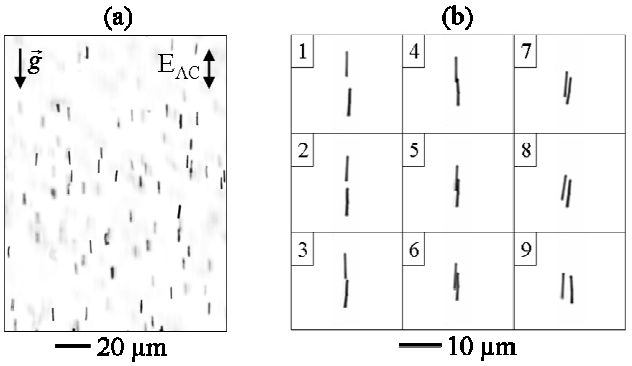

FIG. 4. (a) Image of 6-μm particles aligned in a 100 Hz ac field as they settle through the flow cell and experience hydrodynamic interactions with other particles. The particle density shown here (approximately 10^9 particles/mL) is typical for the experimental measurements and enables image-based detection and tracking of individual particles while ensuring significant particle-particle interactions. For each experimental measurement we track the displacements of all particles in 25,000 images. (b) Experimental example of the typical interaction between two particles due to ICEO driven hydrodynamic interactions. The consecutive series of images shows the time-lapse motion as the particles align end-to-end, slide next to one another, then push apart from their centers.

square displacement of the particles due to the influence of hydrodynamic interactions. The short time dispersion, defined as

$$\mathbf{D}_s = \frac{1}{2\Delta t}\langle[\mathbf{x}(t_n) - \mathbf{x}(t_{n-1})][\mathbf{x}(t_n) - \mathbf{x}(t_{n-1})]\rangle, \qquad (21)$$

describes the variance in particle displacements over a fixed time step Δt. The diffusion coefficients $D_\perp$ and $D_\parallel$, where

$$D_\parallel = \frac{kT\ln(2/\alpha)}{4\pi\eta c} \qquad (22)$$

is the diffusivity parallel to the particle's major axis, provide reference values for the magnitude of the dispersion. The dispersion is a measurable quantity which enables direct comparison between the simulations and experiments.

III. EXPERIMENTAL PROCEDURE

We performed experiments quantifying the hydrodynamic interactions of metal rodlike particle suspensions in electric fields. An ac electric field aligns the particles in a vertical flow channel, minimizing time-averaged translation due to electrophoresis and particle interactions with the channel walls. Figure 4(a) shows a representative image of the particles aligned in the flow channel as they settle. We maintain particle concentrations between 10^8 and 10^9 particles/mL (in 21 μS/cm conductivity solutions) to ensure and study particle-particle interactions due to induced charge electroosmosis. The time-lapse frames in Fig. 4(b) show an example of the typical "aligned overspeeding" then "lateral separation" interactions observed between particles. We quantify particle positions, orientations, and interactions using custom particle image recognition and tracking routines. The experimental setup and particle tracking routines used here have been described in detail by Rose *et al.* [3]. We summarize here some of its major components and parameters.

TABLE I. Parameters for the experiments quantifying hydrodynamic effects due to ICEO.

Length (μm)	Particle concentration (part./mL)	Induced zeta potential (mV)	Pe	Field (V/cm)
6	10^9	0	0	0
		7.5	183	25
		15	732	50
		22.5	1646	75
		30	2927	100
8	10^8	0	0	0
		7.5	228	18.75
		15	912	37.5
		22.5	2052	56.25
		30	3649	75

We visualized the ICEO particle interaction experiments in a 100 μm by 1 mm rectangular cross section capillary (Vitrocom, Mountain Lakes, NJ). The borosilicate capillary was 4.4 cm in length and mounted vertically in a custom acrylic fixture. The metal microrods were pure silver Nanobarcode® particles (Nanoplex, Menlo Park, CA) with specific gravity of 10.5, lengths of 6 and 8 μm $\pm$ 30 nm and diameters of 318 nm $\pm$ 50 nm [1,24]. The suspension solution for the particles was potassium chloride solution (0.14 mM, pH 5.3, 21 μS/cm) with no surfactants added. We maintained the particle number density at 10^8 particles/mL ($nc^3 = 6.4 \times 10^{-3}$) for all experiments with 8 μm particles and 10^9 particles/mL ($nc^3 = 2.7 \times 10^{-2}$) for all experiments with 6 μm particles.

The imaging system was identical to that described by Rose *et al.* [3]. We chose the applied field values based on the induced zeta potential across the particle, $\zeta_s = cE_\infty$, assuming the particle is aligned parallel to the applied field. The selected field values achieve induced zeta potential values from 0 to 30 mV for each particle length. These induced potentials are well below the voltage drop required to initiate electrochemical reactions at the surface of the particles. The driving frequency for the applied fields in all experiments was 100 Hz. Note this frequency is significantly lower than the limiting double layer response frequency (order 1 MHz) discussed in Sec. II C. Table I includes the full data matrix as well as the calculated Peclet number values from Eq. (20).

We obtained a total of 1061 images at 20 fps for each experiment and performed 25 such experiments for each particle length and field strength combination. Before starting the first experiment, we loaded the particles in the capillary using syringe generated pressure, plugged the capillary, and waited at least two minutes to allow the flow to stabilize. We then applied the electric field and began imaging the particles. The particle settling velocity is on the order of microns per second, ensuring a typical particle is imaged roughly 25 times before settling a distance equivalent to its

length. The total number of particle displacements is on the order of 2.5×10^5 for a given particle length at each field strength.

Using a custom particle tracking code, described in detail in Ref. [3], we analyzed each particle image to find the major axis angle and the coordinates of the particle image centroid. The code analyzes the projection of the particle orientation onto the image plane (the depth of field was 2.8 μm). After determining the particle location and orientation, the routine identifies individual particles across images using a "best match" algorithm. We describe further measurement details for specific particle-particle interaction measurements in Sec. IV.

IV. RESULTS AND DISCUSSION

We analyzed our simulation data to determine particle trajectory ensembles, pair distribution functions, and dispersion coefficients. For all simulation results, we used the three-dimensional data for particle locations and velocities assuming the flow fields and motion are axisymmetric about the major axis of a particle. We compare these measurements to the two-dimensional data from the experiments.

A. Simulations results

We analyzed particle trajectories for a suspension of particles with a prescribed Pe of 3000. At this Pe value, the particles align nearly uniformly parallel to the field and the ICEO induced flow field is symmetric. For each particle in the suspension, we fixed its center at the origin then determined the locations of all other particles within the suspension with respect to the fixed particle. We calculated the displacements of nearby particles at every time step and converted these displacements to velocities. To increase the density of velocity vectors, we condensed all the data to a single quadrant then mapped it onto a fixed grid with a $0.2c$ spacing in both dimensions. We then calculated streamlines for the particle motion based on the velocity field.

Figure 5(a) shows the velocity field for the simulated Brownian, high density particle suspensions. The figure also shows several computed streamlines which cross the regions of high velocity as a visual aid. These velocity fields are averaged in time and across all of the particles in the simulation. The average particle motion is consistent with the quadrupolar flow pattern described in Fig. 3 for rodlike particles with an ICEO slip velocity. In the multiparticle simulations of Fig. 5(a), time-averaged ICEO draws liquid into the ends of particles approximately aligned with the field and expels liquid perpendicularly away from their midsection. For sufficient particle density, this induced hydrodynamic flow enhances particle-particle interaction and thereby enhances effective particle dispersion. As described anecdotally in Fig. 4(b), this flow often causes particles to be drawn towards one another at the ends and pushed apart at their centers. As expected, the largest velocity magnitude appears near the particle surface due to the ICEO slip velocity driving the hydrodynamic disturbance.

We determined the pair distribution functions for suspensions with Pe values of 0, 80, and 1600. To calculate the pair distribution functions, we analyzed each particle in the suspension and fixed its center at the origin. We then determined the locations (and orientations) of all other particles within the suspension with respect to the fixed particle. We repeated this at every time step and binned the data to create a two-dimensional histogram of relative particle locations, and this histogram was ensemble averaged with those of all other particles. The simulations show that low electric fields produce an approximately axis-symmetric depletion region (low values in the pair distribution function) near $x=z=0$ as shown in Fig. 6(a). In this regime, particle positions are determined by steric interactions associated with the Brownian sedimentation dynamics. Figures 6(a)–6(c) show how this depletion narrows in the x direction and elongates in the z direction as the field increases. This depletion region corresponds to the excluded volume due to the steric interactions of the (increasingly better aligned) particles. As Pe increases in Fig. 6(b), the depletion region is roughly twice as long along the z axis as it is along the x axis due to enhanced particle alignment. As Pe number reaches 1600 in Fig. 6(c), a region of high particle density develops, seen as the high intensity values framing the particle and covering the regions near the (top) end of the particle and extending down to about $z/2c=0.2$. This distribution shows low values very near the particle axis (as expected due to steric exclusion), but then relatively high values just off the particle axis (indicating "paired" vertical particles). The high particle density region above the end of the particle spans from about $z/2c=1.1$ to 1.4 and with a width of approximately $x/2c=0.15$. This high density region also extends down along the space next to the particle in a high intensity ridge centered at $x/2c=0.2$ (a particle axis-to-axis distance of about eight diameters) and spanning from about $z/2c=0.2$ to 0.8. The latter high intensity region abruptly drops within about 0.3 particle lengths of the $z=0$ midplane, indicating an

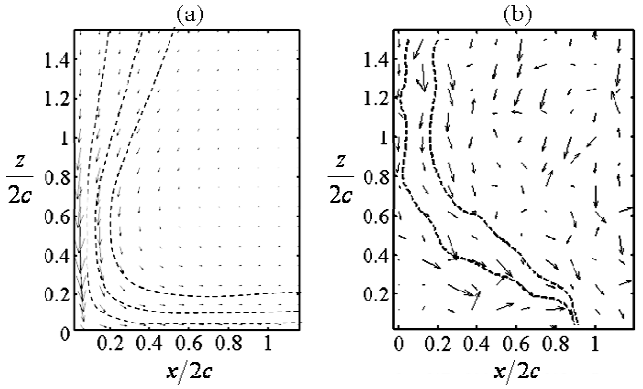

FIG. 5. Vector plots for the trajectory of 6 μm silver particles in a 100 Hz ac field with respect to another particle fixed at the origin and aligned vertically. (a) Simulation measurements for particle trajectory at Pe=3000, such that the particles are nearly completely aligned in the field. The simulation predicts the ICEO flow field around the particles will pull them together at their ends and push them apart at their centers. (b) Experimental trajectory measurements at Pe=2930 show similar trends to the simulations with the second particle typically coming in from the top then being pushed out as the particles slide next to one another.

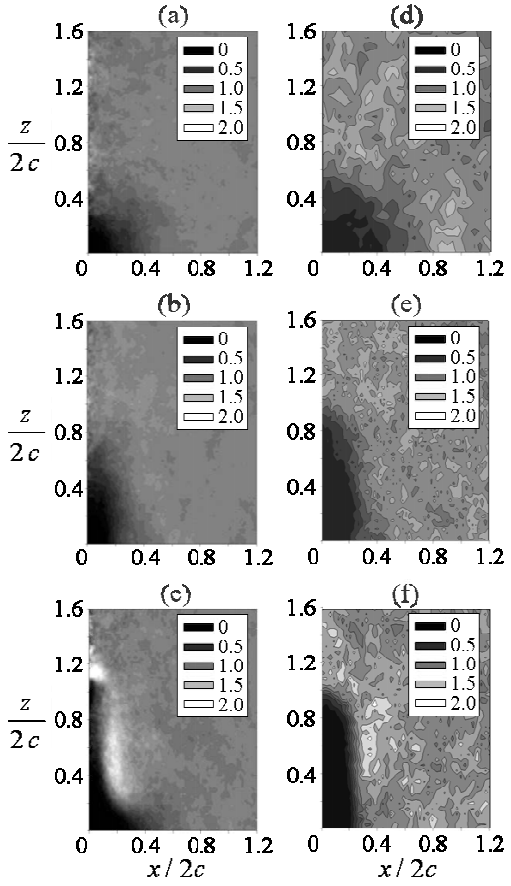

FIG. 6. Pair distribution functions for particles with aspect ratio $\alpha=0.05$. The Pe values were 0, 80, and 1600 for simulations (a)–(c) and 0, 180, and 1650 for the corresponding experiments (d)–(f). The dark region along the vertical axis is due to a combination of excluded volume in which the particles cannot physically overlap and depletion due to the hydrodynamic interactions. The additional depletion in (f) is likely due to limitations in the image processing algorithm. The bright regions around the particle in (c) and (f) demonstrate proof of particle pairing in the simulations and experiments.

axisymmetric depletion region centered near $z=0$. These accumulation and depletion regions are consistent with many "aligned overspeeding" and "lateral separation" events as described in Fig. 4(b). ICEO liquid flows promote end-to-end overspeeding and pairing, followed by relative motion of "paired" particles along the axis, and finally a separation due to the outwash of the near-particle-center ICEO flow.

The dispersion dynamics of the suspension provide insight into suspension stability. We calculated dispersion from the variance of the displacements for all particles within the suspension across all time steps as described in Eq. (21). The calculated dispersion values D_x and D_z are equal to $\sigma_x^2/2\Delta t$ and $\sigma_z^2/2\Delta t$, respectively, where σ^2 is the variance of the displacements in the x or z direction and Δt is the simulation time step. We normalize the measured effective dispersion values of the suspensions by the theoretical diffusivity perpendicular to the particle axis [Eq. (19)]. Figure 7 shows the dispersion for simulations with concentrations of 1×10^7, 1×10^8, and 1×10^9 particles/mL and Pe values ranging from

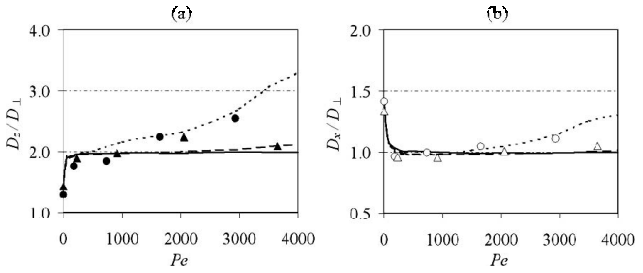

FIG. 7. Comparison of experimental and simulation dispersion measurements for 6-μm and 8-μm particles over the same Pe range. (a) Dispersion measured parallel (z direction) to the direction of the applied field (parallel to the gravity vector). (b) Dispersion measured perpendicular (x direction) to the direction of the applied field. The simulation data is represented in both (a) and (b) by a solid line (—) for particle concentrations of 10^7 particles/mL, long-dashed line (– –) for 10^8 particles/mL, and short-dashed line (---) for 10^9 particles/mL. The triangle and circle markers represent experimental measurements for particle concentrations of 10^8 and 10^9 particles/mL, respectively.

0 to 4000. We first describe the low field and moderate field behaviors of the data where ICEO interactions are negligible. At Pe=0, corresponding to no applied field, the dispersion is approximately the same in the x and z directions as expected due to associated random orientations. The curves in both plots therefore originate at a dispersion ratio of about 1.4. As the field increases, the particles align with the field (parallel to the z axis) so that their measured dispersion is now anisotropic, i.e., lower in the x direction than the z direction, respectively. Near Pe=200, the simulations for $D_z/D_\perp$ and $D_x/D_\perp$, respectively, show rapid increase and decrease to the theoretical values of 2.0 and 1.0 (assuming a perfectly aligned particle). For the lowest concentration of 1×10^7 particles/mL, the data then level off at these values for the Pe range studied here.

Figure 7(a) shows how $D_z/D_\perp$ rapidly increases to a value of 2.0 consistent with the ratio of particle diffusivities parallel and perpendicular to the primary axis [Eqs. (19) and (22)]. For Pe above about 500, the high particle density (1×10^9 particles) simulations show the most significant departure from the single-aligned-particle theory. The deviations exceed the baseline value by 65% as Pe reaches 4000. Significant deviation from single-particle theory occurs for the midrange particle density of 1×10^8 particles/mL, but only above about Pe=3000 (reaching only 8.5% above the baseline at Pe=4000). At high Pe values, ICEO is enhancing particle-to-particle interactions and significantly increasing the effective axial dispersion coefficient D_z.

Figure 7(b) shows the initial rapid decrease of $D_x/D_\perp$ to a value of unity showing that the majority of x displacements are perpendicular to the aligned particle. The high particle density simulations show that $D_x/D_\perp$ deviates from single-particle theory, but the effect is not as pronounced as that of $D_z/D_\perp$. For a concentration of 1×10^8 particles/mL, the simulations show negligible increase of $D_x/D_\perp$ in the x direction as Pe increases. For the highest particle concentration, 1×10^9 particles/mL, dispersion in the x direction begins to deviate from the baseline value as Pe exceeds about

1500, reaching approximately 30% above the baseline value at Pe=4000.

B. Experiments

Using image data of particles as they settle, we obtained ensemble measurements for the properties of suspensions with concentrations of 10^8 and 10^9 particles/mL for five electric fields. Because the images are two-dimensional projections with only a 2.8 μm depth of field, we assume all detected particles are on the same plane. We define the coordinates of the images identically to those described for the channel, with the z axis aligned with gravity (vertical) and the x axis parallel to the image plane (horizontal). To achieve a relatively thin EDL without inducing particle agglomeration, we suspended the particles in 0.14 mM KCl solution. The double layer thickness for this solution was approximately 26 nm, resulting in a λ_D/b ratio equal to 0.17.

We calculated the trajectory of 6 μm long particles in a 100 Hz, 100 V/cm ac applied field (Pe=2930) from the particle displacements between images. For each particle in an image, we fixed the origin at the center of the particle and measured the distance to all other particles. The particle displacements between images determined the velocity magnitudes and directions for particles within two particle lengths. We mapped the velocities from all images onto a fixed, regular grid with a $0.25c$ spacing in both dimensions and present these results in Fig. 5(b). As with the simulation data, we folded and added the experimental data from the four quadrants into a single quadrant ensemble to maximize statistical certainty. From the velocity field, we calculated two streamlines originating at $(x/2c, z/2c)=(0.05, 1.5)$ and (0.2, 1.5).

The experimental velocity vector plot exhibits similar characteristics to the simulations (including the general circulation pattern), although it contains substantial measurement noise. As in the simulation, the average velocity vectors and the streamlines are consistent with particles being drawn together at their ends and pushed apart at their center. Note the region between $0<x/2c<0.3$ and $0<z/2c<0.3$ is a region of very low particle probability (see Fig. 6), making it very difficult to obtain reliable particle vector measurement statistics. This is likely due to both the hydrodynamics creating a depletion region in the area and the limits of the image processing code in distinguishing and successfully identifying particles in this close proximity. We also note that further decrease of statistical uncertainty in these measurements is very difficult. For example, the measurements of Figs. 5–7 collectively show results obtained from more than 10^7 individual particle displacement measurements.

We determined the pair distribution functions for 6-μm-long particles in ac applied fields with amplitudes of 0, 25, and 75 V/cm. These amplitudes correspond to Pe values of 0, 180, and 1650 and are very close to the Pe values used for the simulations. For each particle in an image, the origin was fixed at the center of the particle and the locations of all other particles within the image were determined. This data was recorded for all particles in each of the 25,000 images for a given field strength. A two-dimensional histogram combines the data into bins with the bin size set to ensure an average of 200 particle centers per bin. The two-dimensional histogram is normalized by the particle count in bins from the far-field region. The data is presented as a contour plot of this histogram and shown in Figs. 6(d)–6(f). The experiments show a narrowing of the depletion region near the z axis as the field increases. As in the simulations, for Pe=0, a symmetric depletion region develops in the region between $0<x/2c<0.25$ and $0<z/2c<0.25$, corresponding to steric interactions of the randomly oriented particles. As the Pe number increases a region of high particle density develops near the particle end and along most of its length. This is accompanied again by a strong depletion region near the particle center (where particles often quickly push away from each other). The larger depletion region in the experimental data may be partially due to limits of the image processing code in distinguishing particles in this proximity. Despite these limitations, the simulations and experiments are in relatively good agreement across this Pe range.

To determine the effects of hydrodynamic dispersion on the suspended particles, we measured the dispersion in 100 Hz ac applied fields for 6- and 8-μm long particles at concentrations of 10^9 and 10^8 particles/mL, respectively. We selected the field strengths for each particle length to vary the potential drop $E_\infty c$ between 0 and 30 mV. This value corresponds to an estimate of the induced zeta potential and Table I provides the corresponding Pe value. To determine the dispersion, we calculate the variance of the displacements for all particles in all 25,000 images at a given field strength. As described for the simulations, the dispersion values D_x and D_z are then equal to $\sigma_x^2/2\Delta t$ and $\sigma_z^2/2\Delta t$, respectively, where σ^2 is the variance of the displacements in the x or z direction and Δt is the time between images. The dispersion values are shown in Fig. 7 and normalized by the theoretical diffusivity perpendicular to the particle's major axis. As in the simulated cases, for zero applied field (Pe=0) the experimentally measured dispersion is approximately the same in the x and z directions. Near Pe values of approximately 200, the experimental data shows the same rapid adjustment to the respective theoretical values of 2.0 and 1.0 for $D_z/D_\perp$ and $D_x/D_\perp$, respectively. The experimental data also agrees with the predicted high Pe value trends. The experimentally measured dispersion in the z direction [Fig. 7(a)] has the highest increase in $D_z/D_\perp$ for the highest particle concentration (10^9 particles/mL), in agreement with the simulated results. Measurements for the 10^8 particles/mL concentration show scatter about the expected value, but do not show a trend of significantly increasing $D_z/D_\perp$, also in agreement with the simulations. The measured $D_x/D_\perp$ data [Fig. 7(b)] show no significant deviation from the theoretical value of 1.0 for aligned particles, again consistent with the predicted trend. Overall, the increase in the dispersion coefficient value as Pe increases is attributable to strong quadrupolar flows induced in higher electric fields, resulting in higher fluctuations in particles displacement. As these results demonstrate, the dispersion coefficient increases with higher particle concentration and field.

In the simulations and calculations described above, we neglect any effects of a native zeta potential which may be present on the particles. The model can easily be extended,

however, by including a uniform or nonuniform native zeta potential in Eq. (2). In an ac electric field, an axially symmetric particle with a native uniform zeta potential will still not translate, but we do expect two minor differences from the results described above. First, the native zeta potential will skew the symmetry of the net zeta potential (induced plus native) around the particle. This will lead to a flow field that is not symmetric about the particle center compared to Fig. 3. The native surface charge may also affect particle-particle electrical interactions for particle distances on the order of the double layer thickness. Note that most of the interactions we consider here are hydrodynamic as the particles are almost always at least several Debye lengths away.

V. CONCLUSIONS

We described the model for metal rodlike particle suspensions in aqueous solution as these polarize in an electric field and interact. The electric double layer around each particle polarizes and leads to an induced charge electroosmotic slip velocity near the particle surface. This slip velocity drives a toroidal flow field around the particle pulling fluid in at the particle ends and pushing it out near the center of the particle. We simulated periodic suspensions of these particles and include far-field hydrodynamic interactions (including those due to induced charge electroosmosis), gravity force, buoyancy force, and near field lubrication forces. These simulations are based on the work by Saintillan *et al.* [15,16]. Here we presented simulation results where we measured particle trajectories, pair distributions functions, and dispersion values.

Experimentally, we investigated suspensions of 6- and 8-μm-long silver particles with a diameter of 300 nm in externally applied electric fields. We suspended the particles in 0.14 mM KCl solution to ensure a relatively thin electric double layer then imaged the particles as they settled through a vertically mounted glass capillary. We analyzed the images using a custom particle tracking code to detect the centroid location and orientation of all particles within the images. We then matched particles between images to measure displacements and ultimately individual and ensemble averaged particle velocities, pair distributions functions, and dispersion values for comparison versus the simulations.

The particles in the simulations and experiments were observed to experience repeated pairing interactions in which they come together axially with their ends approaching each other, slide past one another, and then push apart at their centers. The simulations capture this motion quite well as demonstrated by the particle velocity vectors and streamlines (see Fig. 5). The experimentally measured velocity vectors and streamlines also show this general pairing motion. The pair distribution functions are also consistent with particle pairing due to the induced flow field near their surface. Experimental and theoretical pair distributions functions were qualitatively in good agreement, both showing regions of pronounced enrichment and depletion consistent with induced charge electroosmosis flows. We also compared the dispersion measurements between experiments and the simulations to determine net effects on the bulk particle suspension. The simulations capture the increase in particle dispersion as the electric field magnitude increases suggesting increased hydrodynamic interactions due to stronger field-induced electroosmotic flows. The simulated and experimental dispersion measurements also demonstrate enhanced dispersion as the particle concentration increases in agreement with simulations and an increased rate of particle-particle interactions.

ACKNOWLEDGMENTS

We gratefully acknowledge the support of the National Science Foundation through Grant No. CBET-0729771. Portions of this work were performed under the auspices of the U.S. Department of Energy by Lawrence Livermore National Laboratory in part under Contract No. W-7405-Eng-48 and in part under Contract No. DE-AC52-07NA27344.

[1] S. R. Nicewarner-Pena, R. G. Freeman, B. D. Reiss, L. He, D. J. Pena, I. D. Walton, R. Cromer, C. D. Keating, and M. J. Natan, Science **294**, 137 (2001).
[2] J. B.-H. Tok, F. Y. S. Chuang, M. C. Kao, K. A. Rose, S. S. Pannu, M. Y. Sha, G. Chakarova, S. G. Penn, and G. M. Dougherty, Angew. Chem., Int. Ed. **45**, 6900 (2006).
[3] K. A. Rose, J. A. Meier, G. M. Dougherty, and J. G. Santiago, Phys. Rev. E **75**, 011503 (2007).
[4] T. M. Squires and M. Z. Bazant, J. Fluid Mech. **509**, 217 (2004).
[5] M. Z. Bazant and T. M. Squires, Phys. Rev. Lett. **92**, 066101 (2004).
[6] N. I. Gamayunov, G. I. Mantrov, and V. A. Murtsovkin, Colloid J. **54**, 20 (1992).
[7] J. A. Levitan, S. Devasenathipathy, V. Studer, Y. Ben, T. Thorsen, T. M. Squires, and M. Z. Bazant, Colloids Surf., A **267**, 122 (2005).
[8] N. I. Gamayunov, V. A. Murtsovkin, and A. S. Dukhin, Colloid J. USSR **48**, 197 (1986).
[9] V. A. Murtsovkin, Colloid J. **58**, 341 (1996).
[10] N. I. Gamayunov and V. A. Murtsovkin, Colloid J. USSR **49**, 543 (1987).
[11] V. A. Murtsovkin and G. I. Mantrov, Colloid J. USSR **52**, 933 (1990).
[12] S. Gangwal, O. J. Cayre, M. Z. Bazant, and O. D. Velev, Phys. Rev. Lett. **100**, 058302 (2008).
[13] A. S. Dukhin and V. A. Murtsovkin, Colloid J. USSR **48**, 203 (1986).
[14] D. Saintillan, Phys. Fluids **20**, 067104 (2008).
[15] D. Saintillan, E. Darve, and E. S. G. Shaqfeh, J. Fluid Mech. **563**, 223 (2006).
[16] D. Saintillan, E. S. G. Shaqfeh, and E. Darve, Phys. Fluids **18**, 121701 (2006).
[17] K. A. Rose and J. G. Santiago, in *Proceedings of the Ninth*

International Conference on Micro Total Analysis Systems (Kluwer Academic Publisher, Boston, MA, 2005).

[18] N. J. Rivette and J. C. Baygents, Chem. Eng. Sci. **51**, 5205 (1996).

[19] J. A. Stratton, *Electromagnetic Theory* (McGraw-Hill, New York, 1941).

[20] M. Z. Bazant, K. Thornton, and A. Ajdari, Phys. Rev. E **70**, 021506 (2004).

[21] A. Jamshidi, P. J. Pauzauskie, A. T. Ohta, J. Huang, S. Neale, H.-Y. Hsu, J. Valley, P. Yang, and M. C. Wu (unpublished).

[22] A. J. Banchio and J. F. Brady, J. Chem. Phys. **118**, 10323 (2003).

[23] B. Hoffman and E. S. G. Shaqfeh, J. Fluid Mech. (to be published).

[24] C. D. Keating and M. J. Natan, Adv. Mater. (Weinheim, Ger.) **15**, 451 (2003).